Enhancement of Lithium-Ion Conductivity in Liquid Crystalline Block Copolymer Electrolyte by Electric Field Alignment

Isaac Álvarez Moisés, Monika Król, Garance Keus, Zhenni He, Alessandro Innocenti, Stefano Passerini, Janne Ruokolainen, and Jean-François Gohy*

ABSTRACT: A block copolymer electrolyte (BCPE) with a liquid crystal and a lithium-ion conductive phase is investigated to assess the influence of an external applied electric field on the bulk morphology and the resulting electrochemical performance. For this purpose, the controlled synthesis of poly(10-[(4-cyano-4′-biphenyl)oxy] decatyl methacrylate)-*block*-(methoxy-poly(ethylene glycol) methacrylate-*co*-glycidyl methacrylate) [P(MALC)-*b*-P(PEGMA-*co*-GM)] block copolymer is performed by reversible addition−fragmentation transfer polymerization. The BCPE containing lithium bis(trifluoromethanesulfonyl)imide as the salt is drop-cast and crosslinked inside an alternating or direct current electric field. Transmission electron microscopy and small-angle X-ray scattering are utilized to study the phase behavior of BCPE and assess the influence of the electric field on the spatial orientation of the microdomains. A hierarchical lam-in-CYL nanostructure with the perpendicular orientation of the mesogenic smectic layers (lam) with respect to the BCPE cylinders (CYL) long axis is identified. Interestingly, the BCPE cast with electric field treatment gives rise to highly ordered cylindrical structures in comparison to the same BCPE without electric field treatment, which in turn exhibits a poorly ordered worm-like morphology. Consequently, a consistent improvement of the ionic conductivity is observed for the electric field-treated polymer, reaching ionic conductivities up to $4.7 \cdot 10^{-5}$ S·cm^{-1} at 60 °C, compared to $6.1 \cdot 10^{-6}$ S·cm^{-1} at the same temperature for the polymer electrolyte cast without an electric field. Surprisingly, for most of the investigated systems, the BCPE microstructure aligns perpendicular to the applied stimuli, which is explained by the movement of the whole liquid crystalline layer rather than by individual mesogen reorientation.

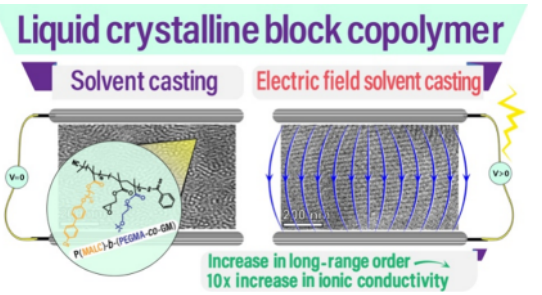

INTRODUCTION

Recently, liquid crystals (LCs) have attracted attention as ion-transport materials because of their molecular self-arrangement.[1−5] One important advantageous characteristic of LCs is their possibility to be aligned by an external electric field (E_F), which is the fundamental principle of LC displays[6−10] and was first studied by Fréedericksz in 1927.[11] The driving force for the alignment induced by an E_F is the orientation-dependent polarization exhibited by a material possessing anisotropic-shaped domains.[12] The director of the LC changes when a static, sufficiently strong E_F is applied.[13] Above a certain field threshold, the director twists until it is aligned with the field. Recently, Wang et al.[14] reviewed the progress in the design of LC electrolytes dedicated for lithium-ion batteries, emphasizing their potential to improve both performance and safety. The key properties of LCs, such as self-assembly, structural order, and responsiveness to stimuli, enable the formation of ordered nanostructured electrolytes with nanoporous channels that facilitate lithium-ion transport. LC electrolytes also offer nonflammability, chemical stability, and enhanced electrode−electrolyte interfaces as compared to traditional liquid electrolytes. Despite these advantages, the widespread implementation of LC-based materials remains hindered due to significant knowledge gaps. The critical challenge lies in the rational design and synthesis of LC molecules tailored for lithium-ion batteries. Furthermore, controlling the morphology of the 3D nanostructures formed by LCs presents significant uncertainty, as the precise manipulation of nanochannel architectures is crucial for optimizing the ion conductivity. Another issue is the long-term stability of the accordingly oriented nanochannels since LCs are typically characterized by a viscous behavior.

One promising approach to circumvent the drawbacks encountered by LC electrolytes is to incorporate them into a block copolymer electrolyte (BCPE), exhibiting microphase-separated nanostructures. Indeed, BCPEs allow one to merge multiple functional properties into one host that are not

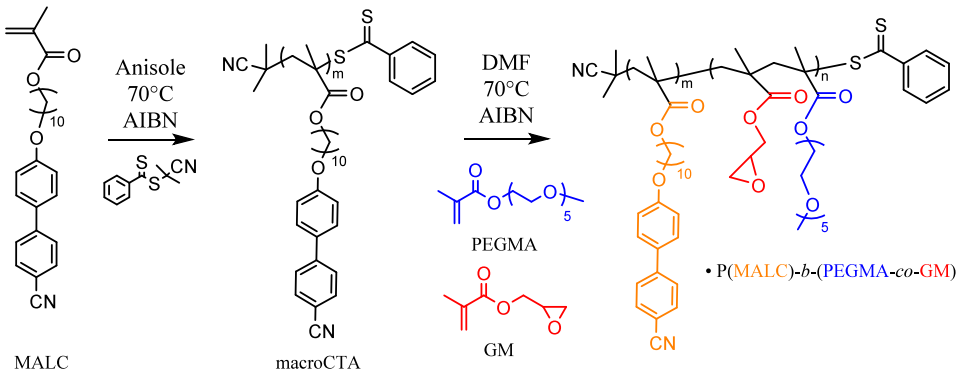

Figure 1. Synthetic route to BCP: the first block is P(MALC), and the second block is a copolymer of PEGMA with GM.

accessible in the monophases, such as a combination of high ionic conductivity with good mechanical stability. It is known that bulk BCPEs tend to self-assemble into different morphologies composed of multiple nanodomains, also called grains. The anisotropy is locally limited to one of the domains, and the global microstructure exhibits a rather isotropic behavior. Achieving the favorable spatial alignment of the conductive nanochannels and the continuity between grains in BCPEs is crucial as such a morphology promotes high ionic conductivity.[15] To fully harvest the potential of BCPEs as a solid polymer electrolyte matrix, different strategies have been developed to align the microstructures.[16,17] More specifically, several studies have been conducted, where LC-containing block copolymer domains were aligned via different stimuli.[18−22] Interestingly, block copolymer melts and solutions are also known to align in the presence of E_F.[21,23−25] The primary reason for this phenomenon is the difference in the dielectric permittivities between the blocks. The configuration where dielectric−dielectric interfaces are perpendicular to the E_F is thermodynamically unfavorable. As a result, the structure tends to reorient itself parallel to the field to reduce the free energy of the system. This behavior contrasts the response of LCs toward E_F, which depends on the dielectric anisotropy of the LC due to differences in the electric permittivity along and perpendicular to its molecular axis.

Therefore, combining in a single material, the response of BCPE microphase-separated nanodomains and LC mesophases toward E_F remains a complex problem. Following this direction, Chao et al.[26] showed that a block copolymer with an LC block containing hydrogen-bonded mesogenic moieties as side chains can be aligned while subjected to alternating current (AC)-generated E_F above the glass transition temperature but below the order-to-disorder temperature. For the parent architecture with covalently bonded LC moieties, directional switching was not possible, which was attributed to the low mobility of the polymeric LC mesophase. Similarly, corresponding systems without LC inclusion did not demonstrate a response to the E_F. They deduced that hydrogen-bonded LC coupled with the presence of free LCs in the system enable swift altering of the spatial orientation of the grains.[26] Mkontha et al.[27] conducted theoretical investigation of the comb-like liquid crystalline diblock copolymer behavior while subjected to E_F. Both LCs with positive and negative dielectric anisotropies were considered. They noted that E_F has a significant influence on the domain spacing of LC BCPs subjected to directed self-assembly, and relatively low E_F can be utilized for systems with high dielectric anisotropy. It was also found that long-range alignment can be achieved if LC ordering precedes the phase separation of BCP. Finally, the use of an AC field instead of direct current (DC) for directed self-assembly via E_F is thought to give more flexibility in the tuning of the system, where most of the issues related to dielectric breakdown, ionic transport, and possible free-ion-induced counter fields should be mitigated.[28,29]

The aim of the present work is to design a solid polymer electrolyte combining LCs and ion-conductive phases in a BCP architecture. Consequently, systems with such a design will be manipulated in E_F and prompted to self-assemble into highly ordered anisotropic functional materials with continuous ion pathways. In order to fix the accordingly obtained E_F-oriented nanostructures, BCPs will be simultaneously crosslinked during the casting process. The microphase behavior of the BCPE will be investigated primarily by small-angle X-ray scattering (SAXS) and transmission electron microscopy (TEM) and further related to their electrochemical performance. The final goal is to demonstrate whether the applied E_F during the casting process can impact the BCPE morphology and improve the ionic conductivity of the obtained material.

RESULTS AND DISCUSSION

The synthetic route toward the BCP as well as its chemical structure are depicted in Figure 1. Briefly, a linear LC block was synthesized through reversible addition−fragmentation transfer (RAFT) polymerization using a chain-transfer agent (CTA). This process involved polymerizing the LC monomer 10-((4′-cyano-[1,1′-biphenyl]-4-yl)oxy)decyl methacrylate (MALC). The LC moiety used in this study, 4-cyano-4′-*n*-decyloxy-biphenyl, is characterized by high positive dielectric anisotropy, which would imply preferred parallel orientation with respect to an applied E_F.[30] Next, the accordingly obtained P(MALC) macroCTA was extended by copolymerizing poly(ethylene glycol) methyl ether methacrylate (PEGMA) with a small amount of glycidyl methacrylate (GM), resulting in P(MALC)-*b*-P(PEGMA-*co*-GM) BCP (Figure 1). GM is introduced as a crosslinker to stabilize the induced structure even after the E_F is turned off. The ion-conductive block is selected for crosslinking to exploit the full potential of E_F-induced ordering of the LC polymer block. Indeed, adding a comonomer to the liquid crystalline block can reduce the ordering of the mesophase.[31] Details of the experimental procedures and characterizations are provided in the Supporting information (SI). The successful synthesis of the starting monomers, P(MALC) macro-CTAs and P(MALC)-*b*-P(PEGMA-*co*-GM), was proven by size-exclusion chromatog-

raphy (SEC) and ^{1}H NMR spectroscopy (Figures S1−S6). The thermal stability was confirmed by thermogravimetric analysis (Figure S7). Various P(MALC) macro-CTAs were obtained, as presented in Table S1. The final composition and macromolecular features of the P(MALC)-*b*-P(PEGMA-*co*-GM) BCP are presented in Table S2.

The liquid crystalline behavior of the MALC and P(MALC) precursors, as well as of P(MALC)-*b*-P(PEGMA-*co*-GM) BCP, was investigated using differential scanning calorimetry (DSC). Two typical thermotropic LC transitions are observed for MALC in Figure S8: a melting peak at 62 °C, corresponding to the transition from a crystalline structure to an LC mesophase, and the transition from the LC mesophase to the isotropic phase at 68 °C. In contrast, P(MALC) displays a melting peak only at 118 °C. P(MALC)-*b*-P(PEGMA-*co*-GM) BCPs show a similar behavior compared to P(MALC) with a melting peak at 118 °C also. Additionally, no glass transition of amorphous PEGMA segments and no melting peak associated with the presence of crystallized PEGMA segments are detected for P(MALC)-*b*-P(PEGMA-*co*-GM), potentially because of the presence of GM comonomers impeding crystallization. At this stage, it is difficult to conclude from DSC results if microphase separation between P(MALC) and P(PEGMA-*co*-GM) blocks occurred, since no transitions from the latter block were detected. However, the observation of the typical transition of the P(MALC) block at 118 °C with no shift for all of the investigated samples suggests that the P(MALC) block is microphase-separated in all samples.

To obtain more information about the LC behavior, polarized optical microscopy (POM) coupled with a heating/cooling plate was used to observe phase changes as a function of temperature in the investigated materials. The samples were first heated to 150 °C, and the POM images were captured at 62 °C during the cooling phase, with a cooling rate of 0.33 °C·min^{-1} (Figure S9). These images reveal the mesomorphic textures of the MALC monomer and the P(MALC) polymer (Figure S9a,b, respectively), highlighting the birefringence of these materials and textures characteristic for LCs, especially smectic mesophases. The observations for MALC fully correlate with the DSC data, which also indicate an LC mesophase at 62 °C. When the temperature was increased above 68 °C, birefringence disappeared, confirming the transition toward an isotropic state. As far as P(MALC) is concerned, a texture characteristic of a smectic mesophase was observed, and isotropization was detected at a much higher temperature (118 °C), suggesting that the polymeric nature of P(MALC) tends to strongly stabilize the smectic mesophase (Figure S9b). It is hypothesized that due to the restricted mobility and topological constraints related to the P(MALC) polymer architecture, MALC moieties are prevented from crystallization at low temperatures and frozen in a glassy structure below the T_g of the polymer. MALC moieties could be arranged in a similar fashion to the LC mesophase, but with less mobility. This lack of sufficient mobility could prevent the observation of a crystalline state to LC mesophase transition by DSC. Since no T_g was observed in the P(MALC) DSC trace, it is, however, difficult to predict at which temperature a real smectic mesophase is formed. Finally, SAXS results at room temperature confirmed the formation of a smectic mesophase layered structure with a period of 4.4 nm between the smectic layers (Figure S10).

BCPE membranes were prepared from P(MALC)-*b*-P(PEGMA-*co*-GM) with and without E_F. This was achieved by mixing them with a lithium salt (lithium bis(trifluorosulfonyl)imide (LiTFSI)), 2,2′-(ethylenedioxy)bis(ethylamine) (EDE) as the crosslinker reacting with the epoxy group of GM, and tetrahydrofuran (THF) as the solvent, followed by solvent-casting. After the drop-casting and curing of the BCPE, the verification of epoxide group transformation was accomplished by Fourier transform infrared (FTIR) spectroscopy. This confirmation was achieved by observing the disappearance of the distinctive band associated with the epoxy groups in the un-crosslinked samples, which occurred at 914 cm^{-1} (Figure S11).[32]

It is worth noting that the block length ratios drastically affect the final properties of the BCPEs. It was determined that the most optimal solution requires establishing a composition that achieves an equimolar distribution of liquid crystalline and ionic conductive phases. BCPEs characterized by an elevated molar ratio of the ionic-conducting block exhibited unfavorable mechanical properties and were unable to attain a self-standing film. Conversely, BCPEs possessing a higher proportion of LC blocks demonstrated brittleness and poor dissociation of the lithium salt.

Microphase separation between P(MALC) and P(PEGMA-*co*-GM) blocks is expected to occur during THF evaporation. In addition, THF was proven to significantly promote faster kinetics of the nanochannels reorientation while subjected to E_F and eliminate problems associated with the high viscosity of the melts.[23,33,34] The use of solvents is particularly advantageous, because it provides mobility to the polymer chains without the need to increase the temperature. As the solvent evaporates in a controlled environment, the chains gradually lose their mobility, and a time window is created during which the polymer chains have sufficient mobility to align. Upon complete evaporation of the solvent, the induced order achieved during the process is preserved. THF also has relatively high polarity, which is thought to stabilize the field-induced polarization of the chains and enable more pronounced chain mobility while the stimulus is applied.[35] In addition, doping one of the blocks with salt is expected to change the phase behavior of the BCP and material response to applied E_F. The presence of free ions in the system is believed to reduce the critical voltage required for reorientation. This is because free ions increase the polarizability of the ion-solvating block, thereby enhancing the dielectric contrast.[36,37] However, if the ion-containing block showed strong affinity to the substrate, a contrary correlation was found.[38]

Various iterations were explored for the morphological characterizations with TEM and SAXS, such as the presence of the E_F, its type (AC or DC), the inclusion of lithium salt, and the addition of EDE for crosslinking. Table 1 provides an overview of the abbreviations and variations in the treatments.

These variations led to distinct morphologies in the resulting BCPs. The same preparation and treatment procedures were used for all of the samples. For example, samples without E_F treatment were placed between quartz substrates without switching on the power source. The experimental setup used to apply E_F during BCP and BCPE membrane formation is depicted in Figure S12. It was necessary to verify that the membranes do not contain significant amounts of THF after the casting, which could mobilize the domains and, hence, decrease the quality of the alignment once the stimulus is removed. Hence, additional NMR spectroscopy was conducted on the films immediately after peeling them off from the

Table 1. Overview of All Combinations Prepared from P(MALC)-*b*-P(PEGMA-*co*-GM): Salt, Crosslinking, E_F (AC or DC)[a]

Sample	Salt	Crosslinking	Electric Field	Acronym
1	X	X	X	S1_Pristine
2	✓	X	X	S1_Salt
3	X	✓	X	S1_CL
4	✓	✓	X	S1_CL/Salt
5	X	X	AC	S1_Pristine/AC
6	✓	X	AC	S1_Salt/AC
7	X	✓	AC	S1_CL/AC
8	✓	✓	AC	S1_CL/Salt/AC
9	X	X	DC	S1_Pristine/DC
10	✓	X	DC	S1_Salt/DC
11	X	✓	DC	S1_CL/DC
12	✓	✓	DC	S1_CL/Salt/DC

[a]A check mark (✓) indicates that the parameter was applied, whereas a cross (X) signifies that it was not applied.

casting setup, and prior to vacuum drying. The results showed no detectable traces of THF, as displayed in Figure S13.

Similar to the previously discussed MALC and P(MALC) samples, POM was used to shed light on the LC behavior of the investigated BCPE membranes. POM images of the investigated BCPEs are depicted in Figure S9c,d. It should be noted that BCP microphase separation between P(MALC) blocks and P(PEGMA-*co*-GM) blocks is expected. This means that the liquid crystalline smectic mesophase formed by the P(MALC) blocks would be limited to microphase-separated nanosized domains. This could easily explain why the usual LC textures (related to micrometer-size LC domains) observed by POM for pure low-molar-mass LC molecules have not been detected here. Figure S9c,d illustrate that the birefringence properties are retained in the BCPEs. This indicates that the MALC mesogen exhibits a robust self-assembly capability, resulting in BCPs with a birefringent texture characteristic of LC behavior, even after doping with LiTFSI and crosslinking.

Finally, S1_CL/Salt/DC was examined under POM to assess the potential changes in birefringence activity with E_F treatment. After E_F treatment, the birefringence tends to disappear due to modifications in the mesogenic order, as illustrated in Figure S9d. This could be due to either an isotropization of the material or the formation of spatially oriented domains (homeotropic ordering). Further SAXS studies will clarify this point.

The temperature-dependent ionic conductivity, a critical parameter for solid-state battery applications, was assessed through PEIS measurements. The resulting conductivity versus temperature curves are presented in Figure 2. As anticipated, all samples exhibited a decrease in conductivity with decreasing temperature, attributable to a reduction in segmental chain mobility at lower temperatures.[39] Notably, the ionic conductivity decreased in the following order: DC-E_F > AC-E_F > no E_F treatment. The enhanced ionic conductivity can be attributed to the morphological changes resulting from the alignment of the BCP and mesogens in response to the DC-E_F, leading to an increase in ionic conductivity for S1_CL/Salt/DC from $6.1\cdot10^{-6}$ to $4.7\cdot10^{-5}$ S·cm^{-1} at 60 °C. The transport of ions is influenced not only by morphological aspects but also by the properties of the ion-conducting block. The Arrhenius model illustrates how the segmental motion of polymer chains is linked to ion transport, showing how both vary with temperature. The conductivity results were fitted by the Arrhenius model using eq 1 over the temperature range of 30−70 °C:[40]

$$\sigma = \sigma_0 \exp\left(\frac{-E_A}{RT}\right) \quad (1)$$

In this context, E_A represents the activation energy for the ion transport. The term σ_0 is a factor that corresponds to the number of charge carriers in the electrolyte. R stands for the gas constant and T the absolute temperature in Kelvin. The activation energy calculated from the Arrhenius plot shows consistent E_A values ranging from 64 to 65 kJ·mol^{-1}, as depicted in Figure 2a,b. Considering that the composition and properties of the compared samples are the same, this phenomenon can be attributed to the unchanged conduction mechanism involving the ion-hopping of lithium ions between neighboring ethylene oxide groups in the P(PEGMA-*co*-GM) phase and a possible ionic conduction mechanism in the P(MALC) LC phase (see the investigation on this possible mechanism). Impedance spectroscopy and chronoamperometry techniques were utilized to measure the transference number t_{Li+} of the sample showing the highest ionic conductivity, i.e., S1_CL/Salt/DC in Li/BCPE/Li coin cells. The current−time curves of DC polarization and AC impedance responses, representing the initial and steady-state current conditions, are presented in Figure S14. The transference number was determined to be t_{Li+} = 0.47 for S1_CL/Salt/DC. This value can be considered relatively high, especially when compared to the Li^+ in PEO-based systems, which typically ranges from 0.2 to 0.3.[41]

The cyclic stability of S1_CL/Salt/DC in contact with lithium metal was investigated by using symmetrical Li/BCPE/Li coin cells at a temperature of 60 °C. The results are depicted in Figure S15. It is evident that the sample exhibits a remarkably low overpotential, approximately 50 mV at a current density of 0.1 mA·cm^{-2}. Furthermore, the cell demonstrates a rather stable overpotential with no indications of short circuits or detectable failures even after 1000 cycles of operation.

The electrochemical stability window (ESW) of S1_CL/Salt/DC was measured in Li/BCPE/SS cells at a temperature of 60 °C, and the corresponding results are depicted in Figure 2b,c. The BCPE demonstrated a wide ESW. During the cathodic scan, the initial decomposition corresponds to the formation of a solid electrolyte interface, which is subsequently stabilized. This is supported by the lithium stripping/plating results, which reveal a stable interfacial behavior even after several hundred hours of cycling at elevated temperatures. On the anodic side, the electrolyte remains stable up to 4.32 V vs Li/Li^+ at 60 °C.

Due to the known significance of the BCP microstructure in relation to ionic conductivity, morphological characterization of BCPE films was thoroughly conducted using SAXS and TEM. More specifically, SAXS and TEM were systematically used to monitor potential morphological changes caused by the following variables: (i) crosslinking of the PEGMA-containing block, (ii) salt addition, and (iii) applied E_F (AC or DC) during the casting process. SAXS profiles were acquired on as-cast films, where the incident X-ray beam (I_0) was directed out-of-plane and in-plane ($I_0 \| E_F$ and $I_0 \perp E_F$, respectively), at room temperature. In some of the measure-

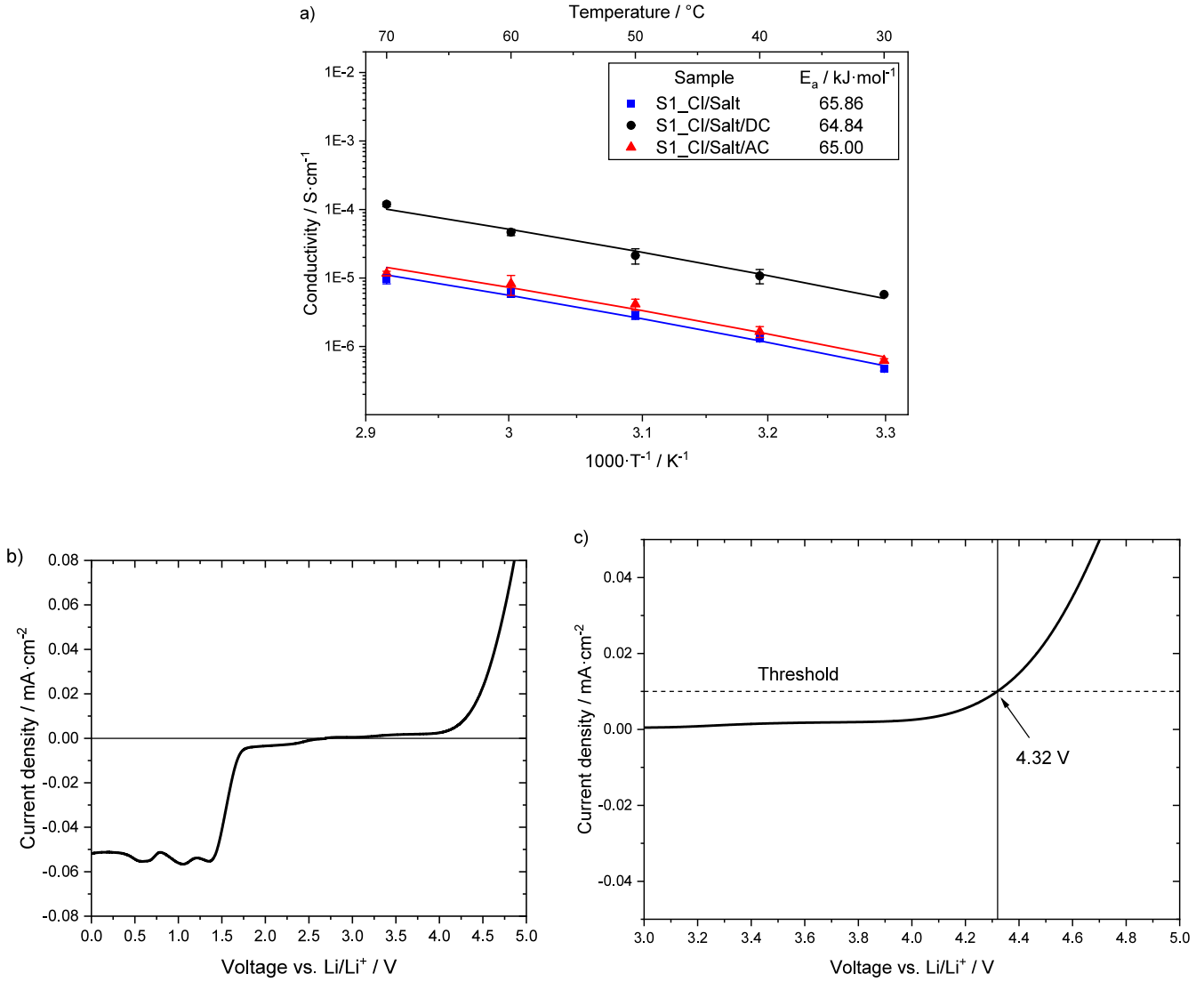

Figure 2. (a) Measurement of ionic conductivity as a function of temperature (ranging from 30 to 70 °C) for the following samples: S1_Cl/Salt, S1_Cl/Salt/DC, and S1_Cl/Salt/AC. These measurements were fitted using the Arrhenius model, as described in eq 1. (b) Linear sweep voltammetry for S1_Cl/Salt/DC. (c) An enlarged view of the anodic scan.

ments, we suspect the artificial contribution of primary beam reflection to the intensity, as membranes were much thinner than the beam spot size. In these cases, the actual circularly integrated intensity $I(\Psi)$ is depicted in dark gray, whereas the integration without this contribution is shown in dashed black lines. The color intensity scales depicted on 2D profiles are arbitrary and readjusted for clarity. The scattering maxima characteristic of the structures originating from BCP self-assembly are marked in black, whereas those for the LC layer smectic ordering are marked in red. The domain (d-) spacing is given by $d = \frac{2\pi}{q^*}$. For lamellar (LAM) morphology, the peak positions were marked as follows $q_h = \frac{2\pi h}{a}$, where h is defined as the first Miller index and a is the lattice parameter. For the cylindrical morphology, the peaks were identified by $q_{hk} = \frac{4\pi\sqrt{h^2+hk+k^2}}{\sqrt{3}\,a}$, where h and k are the first and the second Miller indices, respectively, and a is the lattice parameter.[42,43] TEM micrographs show cross sections of the films in a view parallel to that of E_F. The lighter phase represents the P(MALC) block, whereas the darker one represents the P(PEGMA-*co*-GM) block. Figure 3 provides a short summary of the main findings of this study, comparing S1_CL/Salt and S1_CL/Salt/DC.

Coupled SAXS and TEM measurements effectively highlight the influence of the electric field applied during solvent-casting on the polymer morphology. This directly translates to the improved performance of the materials as ionic conductors. The change was most pronounced in the case of the film prepared in the presence of DC E_F, S1_CL/Salt/DC. A substantial increase of the phase separation degree was observed in comparison to S1_CL/Salt, cast without electric field. This was evidenced by 1D SAXS profiles, where multiple high-order peaks were identified, and TEM, where a poorly ordered worm-like microstructure was replaced by a long-range cylindrical morphology. Highly anisotropic behavior of the examined BCPE was confirmed by analyzing the corresponding $I(\Psi)$, which is elaborated further in the next sections.

The phase-separation patterns and characteristic lengths (d-spacing) of solvent-cast membranes without external stimuli were identified. These findings are detailed in the Supporting Information (SI) section (Figures S16–S20) and are serving as

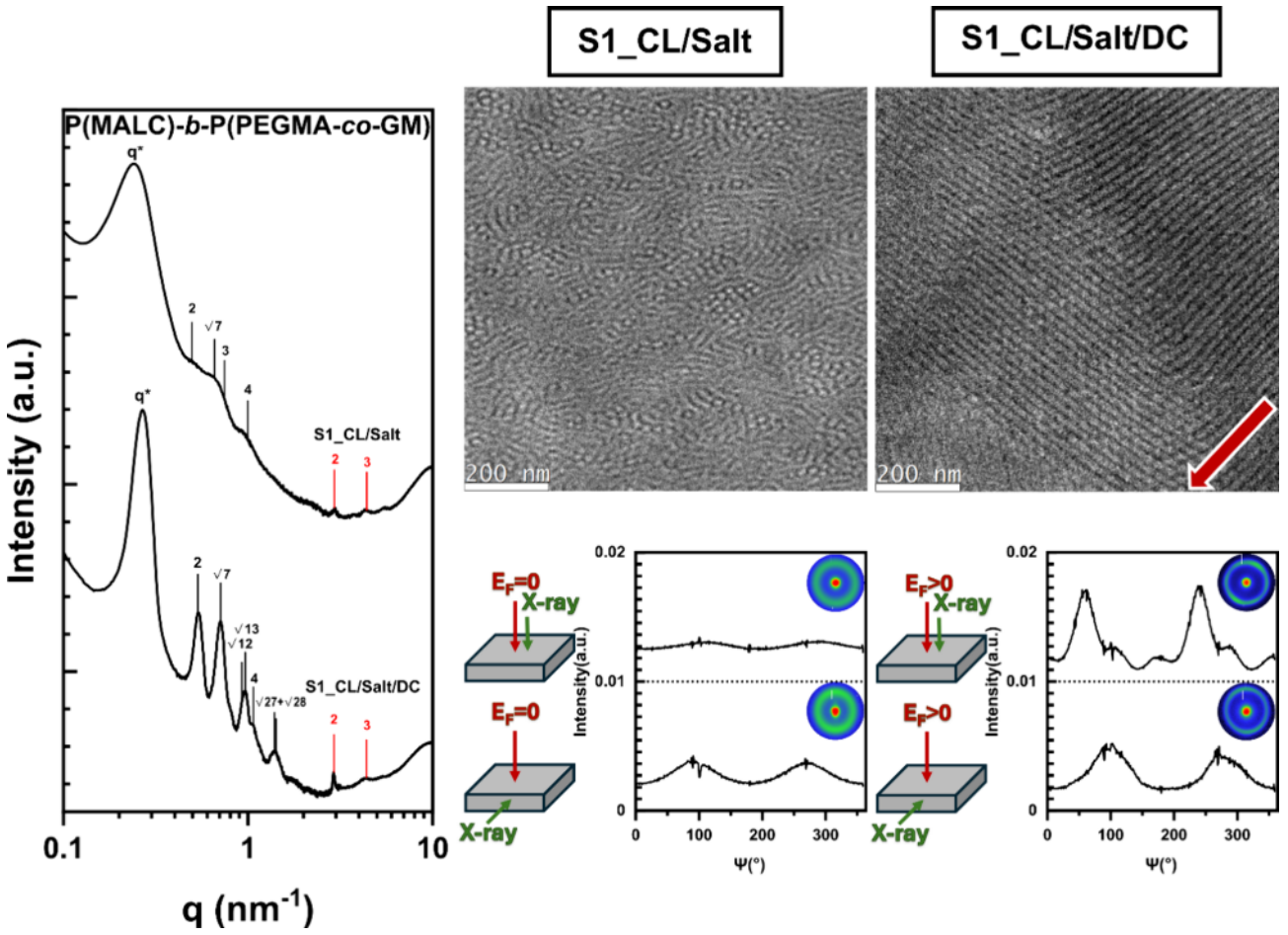

Figure 3. SAXS and TEM data of crosslinked S1 doped with salt in the various casting set-ups. Left: 1D scattering profiles integrated from $I_0 \| E_F$ measurement. Top right: TEM micrographs of corresponding microstructures. Bottom right: $I(\Psi)$ profiles with 2D inserts from $I_0 \| E_F$ and $I_0 \perp E_F$ acquisitions. The red arrow indicates the direction of the E_F.

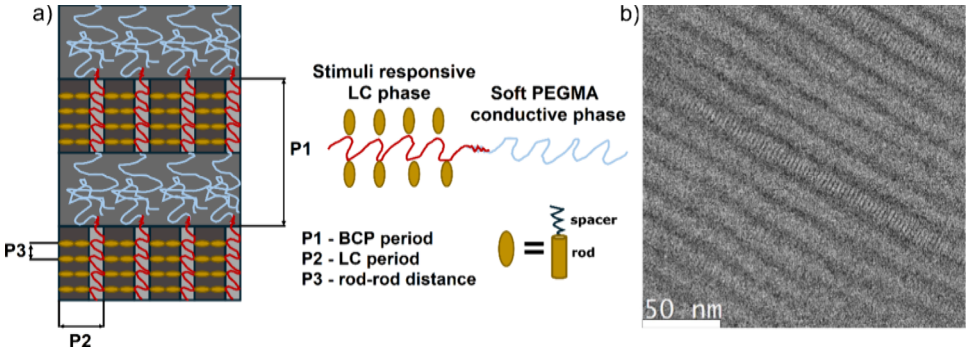

Figure 4. Hierarchical morphology of LC-containing BCPs and BCPEs. (a) Scheme depicting the proposed structure, where LCs anchor homogeneously with respect to the BCP intermaterial dividing surface, resulting in the perpendicular orientation of the smectic layer. (b) TEM micrograph depicting the lam-in-LAM microstructure of S1_Salt/DC with LC layer spacing P2 of 3 nm.

a reference point for further investigations of self-assembly directed by the E_F.

It is well-known that LC-containing systems, with the LC moiety bounded either by covalent or supramolecular bonds, tend to form hierarchical microstructures.[44,23] The self-assembly occurs on two nanoscales: one resulting from phase separation of thermodynamically incompatible constituents of BCP tethered by the covalent bond and the other from the ordering of the anisotropic mesogenic groups. Subsequently, lam-in-LAM or lam-in-HEX structures can be observed. The orientation of the LC layer with respect to BCP could be probed on the E_F-aligned samples. It is important to understand whether phase-separated LC ordering is parallel or perpendicular with respect to the BCP microstructure to examine the LC directional response to the applied stimuli. Here, smectic A ordering of the LC layer, oriented perpendicular to the BCP structure, was identified. To discuss it further, three characteristic length scales and their relative orientation must be noted: P1, which is the period of BCP domains; P2, which is the period of LC layer ordering; and P3,

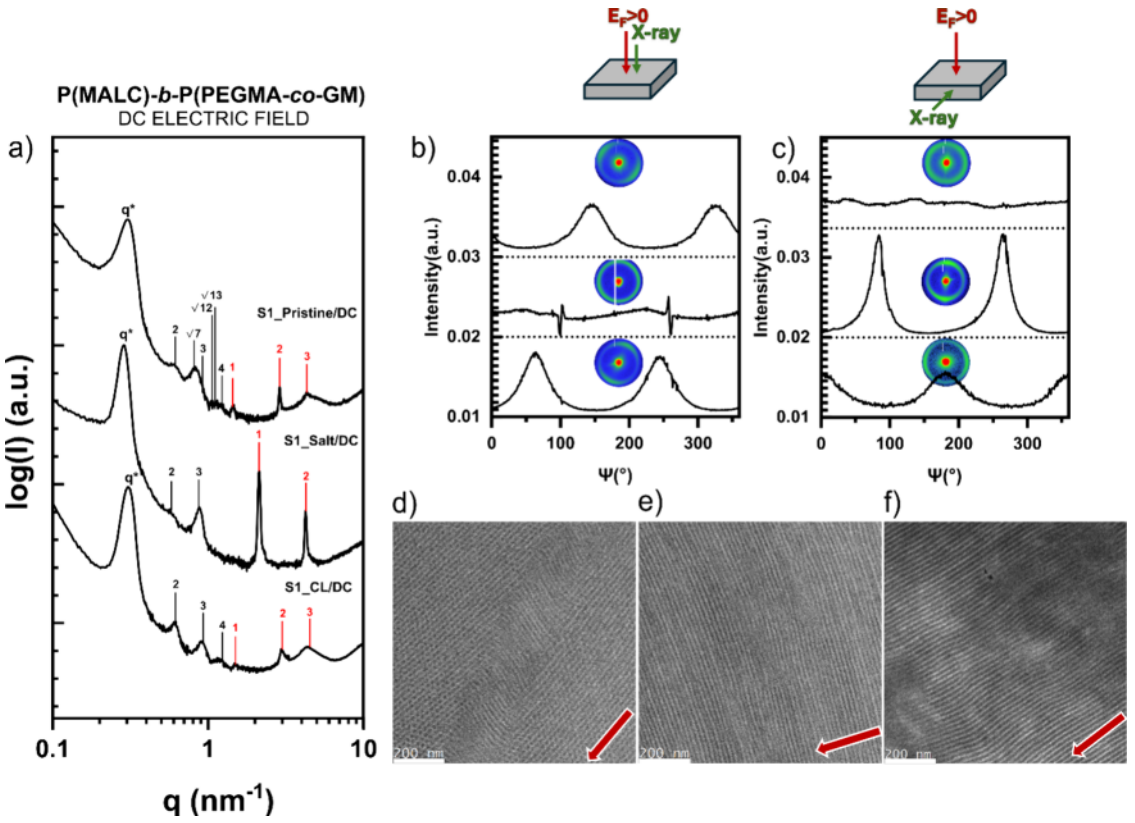

Figure 5. SAXS and TEM data of P(MALC)-*b*-P(PEGMA-*co*-GM) S1 solvent-cast in the presence of DC E_F. (a) 1D scattering spectra azimuthally integrated from $I_0 \| E_F$ measurement. (b) $I_0 \| E_F$ 2D data with the corresponding $I(\Psi)$ profiles. (c) $I_0 \perp E_F$ 2D data with corresponding $I(\Psi)$ profiles. From top to bottom: S1_Pristine/DC; S1_Salt/DC; S1_CL/DC. TEM micrographs of (d) S1_Pristine/DC, (e) S1_Salt/DC, and (f) S1_CL/DC.

which is the rod-to-rod distance. These periods, along with the scheme depicting the prediction of the microstructure, can be seen in Figure 4a.

The smectic period P2 was observed in both cylindrical and lamellar morphologies with a spacing of 4.3 ± 0.1 nm (estimated via SAXS and confirmed via TEM) and is identical with the result obtained for the P(MALC) LC polymer. In the non-crosslinked polymer with salt addition, the smectic period is smaller (3 ± 0.1 nm), as it was shown previously in the corresponding SAXS spectrum of salt-loaded P(MALC) (Figure S10). It is hypothesized that lithium ions migrate into the interlayer spacing between smectic planes due to specific interactions with MALC mesogens, further decreasing the smectic period P2 (see later for further explanation). In Figure 4b, the typical micrograph of the lam-in-LAM structure with a different period P2 of 3 nm is presented, clearly showing the perpendicular orientation of the LC layer (P2) with respect to the BCP (P1). Thus, homogeneous anchoring of LCs in relation to the BCP intermaterial dividing surface can be concluded.

The orthogonal relationship between P2 and P3, indicating the smectic A type of ordering, is shown in Figure S21.

Simple solvent-casting of LC BCP films did not result in the long-range orientation of obtained structures independently of the observed self-assembly nature (LAM vs CYL). The identification of partial preferential parallel stacking of lamellae with respect to the surface via SAXS is attributed to the interfacial interactions between the cast BCPs and PVDF substrate (Figures S18−S20). In this section, the influence of DC-E_F on the BCP domain anisotropy is examined. The morphological characterization of the AC-E_F sample set is available in the SI (see Figures S22 and S23), as a direct comparison with the solvent and DC-E_F films is not possible due to differences in the casting setup (bigger air gap and electric field strength).

DC-E_F alignment was conducted with 1.1 kV·mm^{-1}. Figure 5 depicts SAXS and TEM data belonging to the P(MALC)-*b*-P(PEGMA-*co*-GM) (S1) sample set cast in the presence of DC E_F. The self-assembly nature occurring in S1_Pristine/DC was recognized to be CYL (d= 20 nm) with scattering maxima at q^*, $2q^*$, $\sqrt{7}q^*$, $3q^*$,⋯. LAM microstructures, following the peak positions ratio of q^*, $2q^*$, and $3q^*$, were assumed for S1_Salt/DC and S1_CL/DC, with domain spacings of 22 and 20 nm, respectively. The 1D SAXS data of S1_CL/Salt/DC are shown in Figure 3, which reveals a well-defined high-order scattering pattern at q^*, $2q^*$, $\sqrt{7}q^*$, $\sqrt{13}q^*$,⋯, characteristic for the CYL microstructure, with a d-spacing of 23 nm. It is interesting to note that a possible phase transition of the salt/LC BCP composite microstructure (worm for S1_Salt to LAM for S1_Salt/DC) occurred, while other self-assembled morphologies were preserved.

Coupling TEM data with the azimuthally integrated intensity profiles (Figure 5b,c) gave more in-depth information about the obtained reorientation of the films. Here, the anisotropic 2D patterns reveal a rather mixed response of the systems to E_F. It indicates possible competition of multiple phenomena occurring during directed self-assembly. First of all, quite peculiar circularly averaged patterns from $I_0 \| E_F$ measurements were observed for all samples cast in DC. Usually, an equal distribution of the intensity would be

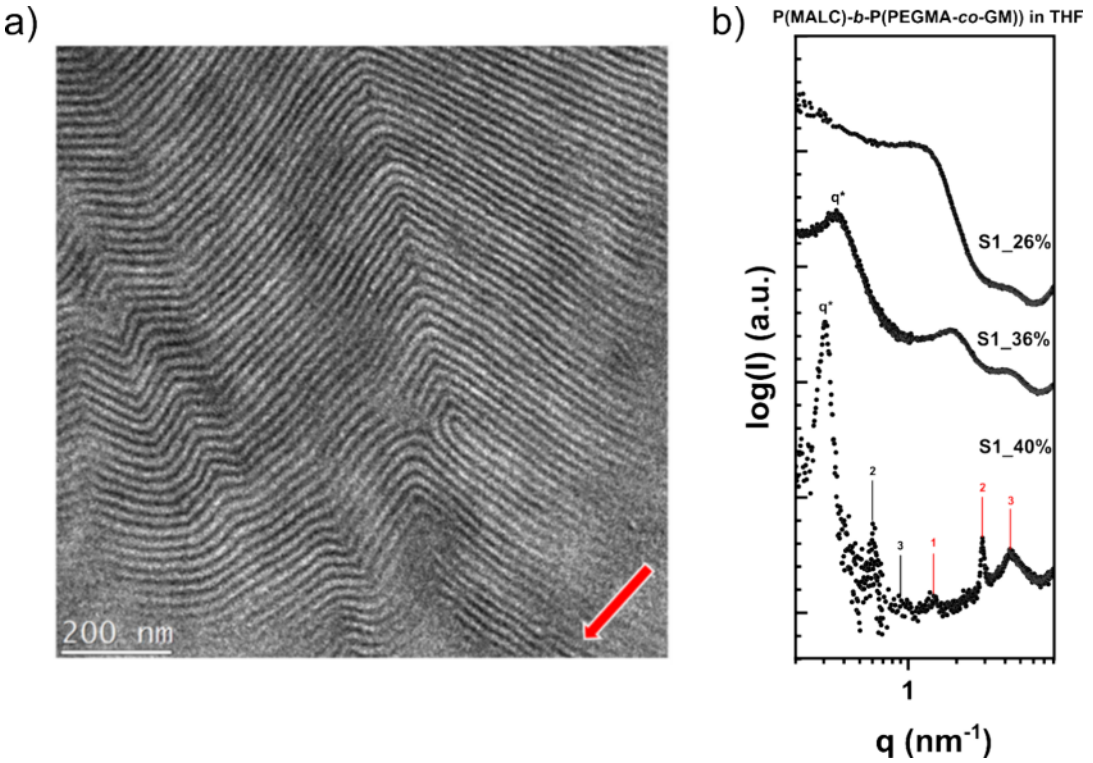

Figure 6. (a) Depiction of the kink defect characteristic for E_F-aligned BCPs, with S1_Salt/DC as an example. The red arrow indicates the E_F direction. (b) SAXS intensity profiles of S1 BCP dissolved in THF at different w/w% concentration points.

expected while directing an X-ray incident beam through the sample volume, independently from the actual directional response of BCP to the stimuli. For the ideal perpendicular alignment with respect to E_F of the LAM system in $I_0 \| E_F$ measurement configuration, most of the planes would not fulfill the Bragg condition. In the case of the ideal parallel reorientation of the grains with respect to the director, azimuthal profiles probed from $I_0 \| E_F$ orientation would be isotropic, as the domains could rotate at any given angle, as long as the LAM/LAM interface is parallel to the E_F. Multiple measurements were conducted on the same sample by systematically shifting the acquisition area by 1 mm, where the obtained profiles are depicted in color in Figure S24b. Therefore, it is concluded that DC alignment gave rise to the relatively big grain size in the investigated systems (or at least bigger than the beam spot size), as the average of those measurements would result in a flat line.

S1_Pristine/DC shows an anisotropic azimuthal profile in the $I_0 \| E_F$ view and rather isotropic 2D pattern in the $I_0 \perp E_F$ view. It could correspond to CYL microstructure, where most of the cylinders are horizontal in respect to the surface; however, their spatial orientation is random within the plane of the film. Such a theory is confirmed by TEM, as shown in Figure 5d, where the increased grain size in comparison to nonaligned samples can be observed. The P(PEGMA-*co*-GM) cylinders are aligned primarily perpendicularly with respect to DC E_F. For S1_Salt/DC, it is also possible to deduce large continuous grains of lamellas aligned perpendicularly with regard to the E_F, as shown in Figure 5e and evidenced by $I_0 \perp E_F$ $I(\Psi)$ data, with sharp peaks located at $\Psi = 90°$ and $\Psi = 270°$. In the case of S1_CL/DC, it was deduced that the grains are primarily oriented in such a way that the LAM/LAM interface is parallel to the stimuli, which is evidenced by both SAXS and TEM, as shown in Figure 5f. S1_CL/Salt/DC I(Ψ) and TEM data are shown in Figure 3. The scattering intensity distribution of S1_CL/Salt/DC shows six intensity maxima in $I(\Psi)$ obtained by recording the scattering intensity with incident X-ray beam parallel to E_F, indicating the preferential orientation of the CYL long axis aligned perpendicular to the director but randomly within the plane of the film. Another possibility is the mix of vertically and horizontally oriented cylinders. The SAXS measurement collected from the thickness of the membranes confirms the presence of the cylinders aligned perpendicularly with respect to the DC field in the examined subset. In this case, the change of the alignment is the most profound: the poorly ordered worm-like microstructure resulted in a long-range ordered HEX morphology. On the micrograph, which represents the side view of the material, two orientations of the cylinder long axis in relation to the E_F can be observed. Compiled data from this sample set are displayed in the SI, Figures S24 and S25.

Despite efforts to decouple as many variables as possible, the examined systems exhibit high complexity. It can be inferred with certainty that the materials were at least partially aligned due to the influence of the E_F, as evidenced by the identification of characteristic kink defects in the electric-field-directed self-assembly, as shown in Figures 6a and S26. These so-called kinks originated from mechanisms associated with the E_F alignment: the grain boundary migration and the grain rotation.[34] Samples aligned by DC field were characterized by the significantly bigger grain size in comparison with AC. The most surprising and quite unexpected phenomenon is that the examined BCP and BCPE tend to align perpendicular to E_F, which is opposite to our prediction and the general consensus regarding the directional response of both BCPs and positive anisotropy

LCs in the uniform E_F. According to our knowledge, the only exception is the work of Elhadj et al.,[45] where authors theorize about the presence of two E_F strength regimes, where one would trap the BCP system in the energy minimum corresponding to the perpendicular orientation; however, their observation is rather empirical. They assigned it to the interfacial effects and initiated heterogeneous nucleation in the presence of E_F. The only exception from the primarily perpendicular orientation of nanodomains are S1-crosslinked BCP and BCPE, where the partial parallel alignment was deduced with respect to the applied E_F. The presence of residual solvent in the system after E_F casting was considered. It was theorized that the chains still retain partial mobility, thus dissipating the order induced by E_F once the stimulus is removed. It would also explain why crosslinked samples partially show the desired parallel orientation with respect to E_F. To investigate this possibility, NMR spectra were acquired on films directly after E_F alignment; however, no significant solvent presence was detected, as shown in Figure S13. It was not possible to confirm any preferential alignment of the mesogenic phase in the case of P(MALC) cast in the presence of E_F (see Figure S27). This could possibly indicate that the main mechanism of BCP and BCPE realignment is not due to the LC director response but due to mere LC presence and the resulting change in the dielectric contrast of blocks. The hierarchical nature of BCPs adds another layer of complexity to the investigated system. Note that TEM micrographs taken at lower magnifications for all of the samples discussed so far are available in the SI in Figures S28−S31.

In the most conventional works, whereas directed self-assembly is conducted in the presence of either electric or magnetic fields, the alignment takes place above the order-to-disorder temperature of BCP and above the isotropization temperature of the LC phase. LC BCP is gradually cooled, accompanied by an external stimulus. The resulting directional formation of the higher-order liquid crystalline mesophase (isotropic to nematic to smectic) is the driving force for the alignment of the whole system.[46,47] In the case of this study, BCPs were dissolved at a low concentration (around 26% w/w), thereby giving chain mobility and disrupting orientational order without requiring elevated temperatures. This approach was motivated by the presence of a temperature-sensitive epoxy moiety. In one scenario, phase separation in the system could be driven primarily by the formation of the LC ordering. It was anticipated that applying an E_F before BCP separation would lead to at least partial alignment of LC directors before they are confined in the LC phase. Alternatively, if phase separation occurred more rapidly than the formation of a highly ordered LC layer, mobile anchored LC molecules would still facilitate the reorientation of the BCP's domain interfaces parallel to the E_F.

To probe the phase separation of both BCP and the LC phase ordering at the different concentration points, an additional study of the S1 BCP polymer phase behavior in THF was conducted, as shown in Figure 6b. Here, it can be initially concluded that the solvent exhibits partial selectivity, as at the lowest BCP concentration (S1_26%), a pattern corresponding to the micellar microstructure can be observed. Upon increasing the concentration of BCP in THF (S1_36%), a rather wide peak at q^* appears and possibly some intermediate mix of weakly phase-separated BCP domains and the residual micelles is present. Finally, at the highest concentration (S1_40%), the peaks position corresponds to the lamellar microstructure with a pronounced, sharp first-order peak. One of the phases is still swollen with the solvent. It is deduced that THF preferentially solvates the P(PEGMA-*co*-GM) block, as S1_Pristine exhibited an inverted CYL microstructure with the P(PEGMA-*co*-GM) being the minor phase.

From the experiment conducted on S1 dissolved in THF, it is concluded that as soon as BCP nanodomain segregation is pronounced, giving rise to phases that can be polarized, the smectic ordering of LC is immediately present. In lower segregation regimes, the LC block is trapped in geometrical morphologies that do not tend to reorient due to the polarization. As mentioned before, the perpendicular orientation of BCP with respect to E_F was resolved by means of SAXS and TEM for the majority of the systems. However, it also proves the simultaneous existence of LC layers parallel to E_F due to the hierarchical nature of BCP self-assembly. Hence, it is theorized that the observed alignment is due to the movement of the whole LC layer rather than due the individual mesogen reorientation. It would mean that the driving force of realignment is the dielectric contrast between the constituents of BCP, where the phase formed by LC has the highest dielectric permittivity and thus aligns parallel to the stimuli. The different responses of the examined chemistries would rely on the interplay of the LC mesophase ordering/BCP phase separation depending on the initial formulation. The evaporation rate of the solvent would also play a crucial role, as it would indicate the time frame in which the chains and respective phases are still mobile and have the possibility to rearrange.

Table S4 summarizes all of the identified microstructures together with characteristic lengths. This comprehensive classification, together with the extended discussion on the analysis of the anisotropic character of the obtained BCPE, can be now related to its performance as an ionic conductor. Here, the following concepts have to be analyzed in order to understand the resulting properties: (i) destructive and nondestructive alignment of the grains with respect to current-supplying electrodes;[15,48] (ii) phase separation strength and the resulting morphology. As highlighted before, the ionic conductivity must be related not only to intragrain transport within the electrolyte microstructure but also to intergrain transport. The importance of the domain orientation and continuity have different impacts depending on the morphology of the considered BCPE. Most of the diblock ionic conductivity models introduce the morphological factor.[48] It accounts for the grains whose spatial orientation is unfavorable for the given morphology type and direction of the conducted current. It is assumed that, on average, approximately 2/3 and 1/3 of the grains contribute to the ion conduction for LAM and CYL (with the ion-conducting block being minority), respectively. In CYL or spherical microstructures, where the majority phase constitutes an ion-conducting block, all grains contribute to the ionic transport. It is also thought that long-range order and stronger phase separation in BCPE promote higher ionic conductivity, as such systems more successfully decouple the functionalities of the constituent blocks. Here, a comparison is made between nonaligned and DC- and AC-aligned crosslinked BCPEs exhibiting CYL morphologies. As proven before, the morphology of these electrolytes exhibits P(MALC) cylinders dispersed in the conductive matrix. It would mean that the

grain orientation is omittable in relating the morphology to the performance of the cast films as ion conductors.

It is assumed that both blocks contribute to ion conduction. This is evident for the P(PEGMA-*co*-GM) block, since it contains ether groups, which are prone to interact with lithium ions and conduct them via the well-known hopping mechanism. As far as the P(MALC) block is concerned, SAXS results discussed earlier have revealed a decrease of the interlayer smectic spacing after salt addition, suggesting interactions between lithium ions and MALC mesogens (Figure S10 and Table S4). These interactions have been evidenced by FTIR spectroscopy (Figure S32), while focusing on the characteristic vibrational band of the nitrile group. The characteristic band at ca. 2250 cm^{-1} appears upon the addition of lithium ions, confirming that nitrile groups have excellent lithium-ion solvating properties.[49]

The liquid crystalline mesogenic layer is oriented orthogonally to the long axis of the cylinder, creating pathways for lithium ions. This effectively makes the ion pathway shorter as there is an intermediate link between the cylinders and the conductive matrix. Then, it is possible to directly correlate the enhancement of the ionic conductivity magnitude to the phase separation strength; systems aligned via DC E_F are characterized by the highest long-range order proven both by TEM and SAXS, as shown in Figure 3. A rather limited and marginal increase of ionic conductivity in the case of AC-aligned BCPEs results from poorer improvement in the phase separation of both BCP and LC phases. Hence, the prompt increase in the ionic conductivity is linked to both stronger phase separation and longer-range order of the grains in comparison to a poorly defined worm microstructure of nonaligned samples and not directly to the favorable BCP grain reorientation with respect to the applied current.

CONCLUSIONS

The synthesis of P(MALC)-*b*-P(PEGMA-*co*-GM) was successfully achieved through RAFT polymerization, and the formation of a smectic A mesophase in a broad temperature range was confirmed for these samples with or without added lithium salt. A setup was developed to drop-cast BCPE solutions into homogeneous E_F (AC or DC) under controlled conditions. Self-standing films were obtained and employed for further electrochemical and morphological analysis. Samples subjected to E_F consistently exhibited enhanced ionic conductivity, reaching values up to $4.7{\cdot}10^{-5}$ $S{\cdot}cm^{-1}$ at 60 °C, compared to $6.0{\cdot}10^{-6}$ $S{\cdot}cm^{-1}$ at the same temperature for the polymer electrolyte cast without E_F. Hierarchical morphologies at two nanoscales were identified across a broad range of examined LC BCP compositions. In all recognized microstructures, the discrete smectic A layers exhibited a perpendicular orientation with respect to the BCP. The influence of the E_F applied during solvent-casting was assessed, revealing that DC fields promote longer-range order and larger grain formation compared to those of AC fields. This effect is attributed to differences in the casting setups used. For AC casting, the voltage was increased stepwise, starting with a lower E_F strength compared to DC casting (0.8 vs 1.1 $kV{\cdot}mm^{-1}$), along with a larger air gap (5 vs 1 mm). It is theorized that the lower E_F applied during the chain mobility window, which depends on the BCP concentration in THF, resulted in a smaller increase in anisotropy and phase separation strength compared to that of the DC-E_F. Surprisingly, the investigated systems were primarily oriented perpendicularly with respect to the E_F. Further fundamental studies are necessary to understand this phenomenon in greater depth. The current working theory suggests that the primary driving force is the dielectric contrast between BCP components rather than LC. As the solvent gradually evaporates, LC rods become trapped in the relatively immobile liquid crystalline mesophase, causing the entire LC layer (not just individual mesogens) to rotate parallel to the stimuli as a phase with potentially the highest dielectric permittivity. The observed increase in ionic conductivity is attributed to the stronger phase separation and longer-range order achieved through E_F-directed self-assembly, which further allow the creation of efficient lithium-ion transport pathways between the different microphases of the BCPE. Solid-state NMR (ssNMR) could provide further insights into the crosslinked network and local chemical environment. Future work may include ssNMR to complement and expand on the current structural analysis.

AUTHOR INFORMATION

Corresponding Author

Jean-François Gohy − *Institute of Condensed Matter and Nanosciences, Université catholique de Louvain (UCLouvain), 1348 Louvain-la-Neuve, Belgium;* orcid.org/0000-0003-4169-1883; Email: jean-francois.gohy@uclouvain.be

Authors

Isaac Álvarez Moisés − *Institute of Condensed Matter and Nanosciences, Université catholique de Louvain (UCLouvain), 1348 Louvain-la-Neuve, Belgium*

Monika Król − *Department of Applied Physics, School of Science, Aalto University, Espoo FIN-00076, Finland;* orcid.org/0000-0003-3804-7990

Garance Keus − *Institute of Condensed Matter and Nanosciences, Université catholique de Louvain (UCLouvain), 1348 Louvain-la-Neuve, Belgium*

Zhenni He − *Institute of Condensed Matter and Nanosciences, Université catholique de Louvain (UCLouvain), 1348 Louvain-la-Neuve, Belgium*

Alessandro Innocenti − *Helmholtz Institute Ulm (HIU), 89081 Ulm, Germany; Karlsruhe Institute of Technology (KIT), 76021 Karlsruhe, Germany;* Present Address: Zentrum für Sonnenenergie- and Wasserstoff-Forschung Baden-Württemberg, Lise-Meitner-Strasse 24, 89081, Ulm, Germany; orcid.org/0000-0003-2902-4068

Stefano Passerini − *Helmholtz Institute Ulm (HIU), 89081 Ulm, Germany; Karlsruhe Institute of Technology (KIT), 76021 Karlsruhe, Germany; Austrian Institute of Technology*

(AIT), Transport Technologies, 1020 Wien, Austria; orcid.org/0000-0002-6606-5304
Janne Ruokolainen − *Department of Applied Physics, School of Science, Aalto University, Espoo FIN-00076, Finland*

Author Contributions

I.Á.M. and M.K. contributed equally to this work.

Notes

The authors declare no competing financial interest.

■ ACKNOWLEDGMENTS

All authors acknowledge the EU's Horizon 2020 Research and Innovation Programme under Marie Skłodowska-Curie Grant Agreement 860403 "POLYSTORAGE" for funding. J.-F.G. is grateful to Service Public de Wallonie (Win4Excellence BATFACTORY 310153 project) for financial support. M.K. and J.R. acknowledge the provision of facilities and technical support by Aalto University at OtaNano-Nanomicroscopy Center (Aalto NMC).

■ REFERENCES

(1) Kuwabara, A.; Enomoto, M.; Hosono, E.; Hamaguchi, K.; Onuma, T.; Kajiyama, S.; Kato, T. Nanostructured liquid-crystalline Li-ion conductors with high oxidation resistance: molecular design strategy towards safe and high-voltage-operation Li-ion batteries. *Chem. Sci.* **2020**, *11* (39), 10631−10637.
(2) Kishimoto, K.; Suzawa, T.; Yokota, T.; Mukai, T.; Ohno, H.; Kato, T. Nano-segregated polymeric film exhibiting high ionic conductivities. *J. Am. Chem. Soc.* **2005**, *127* (44), 15618−15623.
(3) Kato, T.; Mizoshita, N. Self-assembly and phase segregation in functional liquid crystals. *Curr. Opin. Solid State Mater. Sci.* **2002**, *6* (6), 579−587.
(4) Wang, S.; Wang, A.; Yang, C.; Gao, R.; Liu, X.; Chen, J.; Wang, Z.; Zeng, Q.; Liu, X.; Zhou, H.; Zhang, L. Six-arm star polymer based on discotic liquid crystal as high performance all-solid-state polymer electrolyte for lithium-ion batteries. *J. Power Sources* **2018**, *395*, 137−147.
(5) Iinuma, Y.; Kishimoto, K.; Sagara, Y.; Yoshio, M.; Mukai, T.; Kobayashi, I.; Ohno, H.; Kato, T. Uniaxially parallel alignment of a smectic a liquid-crystalline rod−coil molecule and Its lithium salt complexes using rubbed polyimides. *Macromolecules* **2007**, *40* (14), 4874−4878.
(6) Bremer, M.; Kirsch, P.; Klasen-Memmer, M.; Tarumi, K. The TV in your pocket: development of liquid-crystal materials for the new millennium. *Angewandte Chemie (International ed. in English)* **2013**, *52* (34), 8880−8896.
(7) Feng, X.; Tousley, M. E.; Cowan, M. G.; Wiesenauer, B. R.; Nejati, S.; Choo, Y.; Noble, R. D.; Elimelech, M.; Gin, D. L.; Osuji, C. O. Scalable fabrication of polymer membranes with vertically aligned 1 nm pores by magnetic field directed self-assembly. *ACS Nano* **2014**, *8* (12), 11977−11986.
(8) Umeda, M.; Uchida, I. Electric-field oriented polymer blend film for proton conduction. *Langmuir: the ACS journal of surfaces and colloids* **2006**, *22* (10), 4476−4479.
(9) Parshin, A. M.; Zyryanov, V. Y.; Shabanov, V. F. Alignment of liquid crystals by polymers with residual amounts of solvents. *Sci. Rep.* **2017**, *7* (1), 3042.
(10) Helfrich, W. Conduction-induced alignment of nematic liquid crystals: basic model and stability considerations. *J. Chem. Phys.* **1969**, *51* (9), 4092−4105.
(11) Fréedericksz, V.; Zolina, V. Forces causing the orientation of an anisotropic liquid. *Trans. Faraday Soc.* **1933**, *29* (140), 919−930.
(12) Thurn-Albrecht, T.; DeRouchey, J.; Russell, T. P.; Kolb, R. Pathways toward electric field induced alignment of block copolymers. *Macromolecules* **2002**, *35* (21), 8106−8110.
(13) Zocher, H. The effect of a magnetic field on the nematic state. *Trans. Faraday Soc.* **1933**, *29* (140), 945.
(14) Wang, X.; Yan, R.; Niu, H.; He, Z.; He, W.; Miao, Z. Applications of liquid crystal in lithium battery electrolytes. *Journal of Energy Storage* **2024**, *100*, No. 113687.
(15) Majewski, P. W.; Gopinadhan, M.; Osuji, C. O. The effects of magnetic field alignment on lithium ion transport in a polymer electrolyte membrane with lamellar morphology. *Polymers* **2019**, *11* (5), 887.
(16) Kambe, Y.; Arges, C. G.; Patel, S. N.; Stoykovich, M. P.; Nealey, P. F. Ion conduction in microphase-separated block copolymer electrolytes. *Electrochem. Soc. Interface* **2017**, *26*, 61.
(17) Hu, H.; Gopinadhan, M.; Osuji, C. O. Directed self-assembly of block copolymers: a tutorial review of strategies for enabling nanotechnology with soft matter. *Soft Matter* **2014**, *10* (22), 3867−3889.
(18) Majewski, P. W.; Gopinadhan, M.; Jang, W.-S.; Lutkenhaus, J. L.; Osuji, C. O. Anisotropic ionic conductivity in block copolymer membranes by magnetic field alignment. *J. Am. Chem. Soc.* **2010**, *132* (49), 17516−17522.
(19) Tong, Y.; Chen, L.; He, X.; Chen, Y. Sequential effect and enhanced conductivity of star-shaped diblock liquid-crystalline copolymers for solid electrolytes. *J. Power Sources* **2014**, *247*, 786−793.
(20) Zhao, Y.; Qi, B.; Tong, X.; Zhao, Y. Synthesis of double side-chain liquid crystalline block copolymers using RAFT polymerization and the orientational cooperative effect. *Macromolecules* **2008**, *41* (11), 3823−3831.
(21) Adeel, M.; Zhao, B.; Xu, S.; Zheng, S. Investigation of azobenzene photoisomerization effect on morphologies and properties of nanostructured thermosets involving epoxy and a diblock Copolymer. *journal of physical chemistry. B* **2019**, *123* (47), 10110−10123.
(22) Wei, R.; He, Y.; Wang, X. Diblock copolymers composed of a liquid crystalline azo block and a poly(dimethylsiloxane) block: synthesis, morphology and photoresponsive properties. *RSC Adv.* **2014**, *4* (102), 58386−58396.
(23) Tenneti, K. K.; Chen, X.; Pan, Q.; Li, C. Y. Structure and assembly of liquid crystalline block copolymers. In *Liquid Crystalline Polymers*; Zhu, L.; Li, C. Y., Eds.; Polymers and Polymeric Composites: A Reference Series; Springer International Publishing, 2020; pp 173−216.
(24) Pester, C. W.; Liedel, C.; Ruppel, M.; Böker, A. Block copolymers in electric fields. *Prog. Polym. Sci.* **2017**, *64*, 182−214.
(25) Böker, A.; Knoll, A.; Elbs, H.; Abetz, V.; Müller, A. H. E.; Krausch, G. Large scale domain alignment of a block copolymer from solution using electric fields. *Macromolecules* **2002**, *35* (4), 1319−1325.
(26) Chao, C.-Y.; Li, X.; Ober, C. K.; Osuji, C.; Thomas, E. L. Orientational switching of mesogens and microdomains in hydrogen-bonded side-shain liquid-crystalline block copolymers using AC electric fields. *Adv. Funct Materials* **2004**, *14* (4), 364−370.
(27) Mkhonta, S. K.; Elder, K. R.; Huang, Z.-F.; Grant, M. Microphase separation in comblike liquid-crystalline diblock copolymers. *Physical review. E, Statistical, nonlinear, and soft matter physics* **2013**, *88* (4), 42602.
(28) Merekalov, A. S.; Derikov, Y. I.; Artemov, V. V.; Ezhov, A. A.; Kudryavtsev, Y. V. Vertical Cylinder-to-lamella transition in thin block copolymer films induced by in-plane electric field. *Polymers* **2021**, *13* (22). DOI: 3959.
(29) Merekalov, A. S.; Derikov, Y. I.; Ezhov, A. A.; Kriksin, Y. A.; Erukhimovich, I. Y.; Kudryavtsev, Y. V. Orientation control of the hexagonal and lamellar phases in thin block copolymer films using in-plane AC electric field. *Polymer* **2023**, *264*, No. 125544.
(30) Muller, A.H. E.; Yan, D.; Litvinenko, G.; Zhuang, R.; Dong, H. Kinetic analysis of "living" polymerization processes exhibiting Slow

Equilibria. 2. Molecular Weight Distribution for Degenerative Transfer (Direct Activity Exchange between Active and "Dormant" Species) at Constant Monomer Concentration. *Macromolecules* **1995**, *28*, 7335−7338.
(31) Geelhaar, T.; Griesar, K.; Reckmann, B. 125 years of liquid crystals–a scientific revolution in the home. *Angewandte Chemie (International ed. in English)* **2013**, *52* (34), 8798−8809.
(32) Fadlelmoula, A.; Pinho, D.; Carvalho, V. H.; Catarino, S. O.; Minas, G. Fourier transform infrared (FTIR) spectroscopy to analyse human blood over the last 20 years: A Review towards Lab-on-a-Chip Devices. *Micromachines* **2022**, *13* (2). DOI: 187.
(33) Böker, A.; Schmidt, K.; Knoll, A.; Zettl, H.; Hänsel, H.; Urban, V.; Abetz, V.; Krausch, G. The influence of incompatibility and dielectric contrast on the electric field-induced orientation of lamellar block copolymers. *Polymer* **2006**, *47* (3), 849−857.
(34) Böker, A.; Elbs, H.; Hänsel, H.; Knoll, A.; Ludwigs, S.; Zettl, H.; Urban, V.; Abetz, V.; Müller, A. H. E.; Krausch, G. Microscopic mechanisms of electric-field-induced alignment of block copolymer microdomains. *Physical review letters* **2002**, *89* (13), No. 135502.
(35) Sun, Z.; Wang, C. H. Dynamics of polymer chains in solution subject to an electric field probed by quasielastic light scattering. *Macromolecules* **1999**, *32* (8), 2605−2609.
(36) Tsori, Y.; Tournilhac, F.; Leibler, L. Orienting ion-containing block copolymers using AC electric fields. *Macromolecules* **2003**, *36* (15), 5873−5877.
(37) Zheng, B.; Man, X.; Ou-Yang, Z.-C.; Schick, M.; Andelman, D. Orienting thin films of lamellar block copolymer: the combined effect of mobile ions and electric field. *Macromolecules* **2018**, *51* (19), 7881−7892.
(38) Putzel, G. G.; Andelman, D.; Tsori, Y.; Schick, M. Ionic effects on the electric field needed to orient dielectric lamellae. *J. Chem. Phys.* **2010**, *132* (16), 164903.
(39) Landesfeind, J.; Gasteiger, H. A. Temperature and concentration dependence of the ionic transport properties of lithium-ion battery electrolytes. *J. Electrochem. Soc.* **2019**, *166* (14), A3079−A3097.
(40) Peleg, M.; Normand, M. D.; Corradini, M. G. The Arrhenius equation revisited. *Critical reviews in food science and nutrition* **2012**, *52* (9), 830−851.
(41) Evans, J.; Vincent, C. A.; Bruce, P. G. Electrochemical measurement of transference numbers in polymer electrolytes. *Polymer* **1987**, *28* (13), 2324−2328.
(42) Rubatat, L. Block copolymer electrolytes for fuel cells and secondary batteries, the small angle neutron scattering inputs. *EPJ Web Conf.* **2018**, *188*, 3002.
(43) Förster, S.; Timmann, A.; Konrad, M.; Schellbach, C.; Meyer, A.; Funari, S. S.; Mulvaney, P.; Knott, R. Scattering curves of ordered mesoscopic materials. *journal of physical chemistry. B* **2005**, *109* (4), 1347−1360.
(44) Ndaya, D.; Bosire, R.; Vaidya, S.; Kasi, R. M. Molecular engineering of stimuli-responsive, functional, side-chain liquid crystalline copolymers: synthesis, properties and applications. *Polym. Chem.* **2020**, *11* (37), 5937−5954.
(45) Elhadj, S.; Woody, J. W.; Niu, V. S.; Saraf, R. F. Orientation of self-assembled block copolymer cylinders perpendicular to electric field in mesoscale film. *Appl. Phys. Lett.* **2003**, *82* (6), 871−873.
(46) Deshmukh, P.; Gopinadhan, M.; Choo, Y.; Ahn, S.-K.; Majewski, P. W.; Yoon, S. Y.; Bakajin, O.; Elimelech, M.; Osuji, C. O.; Kasi, R. M. Molecular design of liquid crystalline brush-like block copolymers for magnetic field directed self-assembly: a platform for functional materials. *ACS macro letters* **2014**, *3* (5), 462−466.
(47) Gopinadhan, M.; Choo, Y.; Osuji, C. O. Strong orientational coupling of block copolymer microdomains to smectic layering revealed by magnetic field alignment. *ACS macro letters* **2016**, *5* (3), 292−296.
(48) Hallinan, D. T.; Villaluenga, I.; Balsara, N. P. Polymer and composite electrolytes. *MRS Bull.* **2018**, *43* (10), 759−767.
(49) Zhao, Y.; Wang, L.; Zhou, Y.; Liang, Z.; Tavajohi, N.; Li, B.; Li, T. *Adv. Sci.* **2021**, *8*, No. 2003675.